

Active region moss

Basic physical parameters and their temporal variation

D. Tripathi¹, H. E. Mason¹, G. Del Zanna¹, and P. R. Young^{2,3}

¹ DAMTP, University of Cambridge, Wilberforce Road, Cambridge CB3 0WA, UK
e-mail: D.Tripathi@damtp.cam.ac.uk

² Space Science Division, Naval Research Laboratory, Washington, DC 20375, USA

³ George Mason University, 4400 University Drive, Fairfax, VA 22030, USA

Received 16 December 2009 / Accepted 10 May 2010

ABSTRACT

Context. Active region moss are transition region phenomena, first noted in the images recorded by the Transition Region and Coronal Explorer (TRACE) in $\lambda 171$. Moss regions are thought to be the footpoints of hot loops (3–5 MK) seen in the core of active regions. These hot loops appear “fuzzy” (unresolved). Therefore, it is difficult to study the physical plasma parameters in individual hot core loops and hence their heating mechanisms. Moss regions provide an excellent opportunity to study the physics of hot loops. In addition, they allow us to study the transition region dynamics in the footpoint regions.

Aims. To derive the physical plasma parameters such as temperature, electron density, and filling factors in moss regions and to study their variation over a short (an hour) and a long time period (5 consecutive days).

Methods. Primarily, we have analyzed spectroscopic observations recorded by the Extreme-ultraviolet Imaging Spectrometer (EIS) aboard Hinode. In addition we have used supplementary observations taken from TRACE and the X-Ray Telescope (XRT) aboard Hinode.

Results. The moss emission is strongest in the Fe XII and Fe XIII lines. Based on analyses using line ratios and emission measure we found that moss regions have a characteristic temperature of $\log T[\text{K}] = 6.2$. The temperature structure in moss region remains almost identical from one region to another and it does not change with time. The electron densities measured at different locations in the moss regions using Fe XII ratios are about $1\text{--}3 \times 10^{10} \text{ cm}^{-3}$ and about $2\text{--}4 \times 10^9 \text{ cm}^{-3}$ using Fe XIII and Fe XIV. The densities in the moss regions are similar in different places and show very little variation over short and long time scales. The derived electron density substantially increased (by a factor of about 3–4 or even more in some cases) when a background subtraction was performed. The filling factor of the moss plasma can vary between 0.1–1 and the path length along which the emission originates is from a few 100 to a few 1000 kms long. By combining the observations recorded by TRACE, EIS and XRT, we find that the moss regions correspond to the footpoints of both hot and warm loops.

Key words. Sun: atmosphere – Sun: activity – Sun: corona – Sun: UV radiation – Sun: transition region – Sun: magnetic topology

1. Introduction

The high resolution images obtained by the Transition Region and Coronal Explorer (TRACE; Handy et al. 1999) revealed a new type of emission called “moss”. Moss regions are bright, finely textured, mottled, low lying emission above the active region plage area. Moss regions are seen best in the TRACE images obtained at Fe IX/x $\lambda 171$ (Schrijver et al. 1999; Berger et al. 1999). It has been shown that moss regions are always observed in plage regions in the vicinity of hot loops. These features are possibly the same phenomena observed by Peres et al. (1994) using the Normal Incidence X-ray Telescope, where they found that many active regions were associated with low-lying areas of intense emission resembling plage regions seen in H α observations. Using observations from TRACE and the Soft X-ray Telescope (SXT; Tsuneta et al. 1991) it was suggested that the moss regions correspond to the footpoint locations of hot loops which are observed using X-ray images at 3–5 MK (Berger et al. 1999; Martens et al. 2000; Antiochos et al. 2003).

Active regions on the Sun primarily comprise two types of loops; the loops seen in the hot and dense core of active regions in X-ray observations at 2–3 MK (and higher) and the larger loops seen on the periphery of active regions at 1 MK

(see e.g. Del Zanna & Mason 2003). The loops seen on the periphery of active regions are termed “warm loops”. With high spatial resolution instruments such as TRACE, and the Extreme-ultraviolet Imaging Spectrometer (EIS; Culhane et al. 2007) onboard Hinode (Kosugi et al. 2007), the warm loops seem to be spatially well resolved. Using TRACE and EIS observations the plasma parameters (such as electron density, temperature and flows) in warm loops can be measured (see e.g., Warren et al. 2008a; Tripathi et al. 2009).

In contrast, the hot loops in the core of active regions appear quite small, diffuse and difficult to resolve with present day instrumentation. It has also been known for some time that the corona appears “fuzzier” at higher temperatures. (Tripathi et al. 2009) showed that this was not simply an instrumental feature. This effect makes it very difficult to resolve a single isolated loop structure in the core of an active region. As a consequence, it is difficult to study the heating mechanism for individual hot loops. A different approach is therefore required. Since it has been proposed that moss regions are the footpoints of hot loops, a detailed investigation of physical plasma parameters in moss regions and their variation with time should give some indication of the nature of the heating mechanism(s).

In an earlier study (Tripathi et al. 2008), using a single dataset from EIS, we measured the electron densities and magnetic field structures in moss regions. We found that the densities in moss regions were higher than the surrounding regions in the active region and varied within the range 10^{10} – $10^{10.5}$ cm $^{-3}$ from one moss region to the other. In addition, we found that the moss regions were primarily located in only one magnetic polarity region. In this paper, which is an extension of Tripathi et al. (2008), we use observations recorded by EIS to study physical plasma parameters (such as electron densities, temperatures, filling factors, and column depth) in different moss regions within the same active region. In particular, we study the variation of these parameters over short (one hour) and long (5 days) time periods. To the best of our knowledge this is the first time that a spectroscopic study has been carried out to study the variation of physical parameters in moss regions over a short and a long period of time.

The rest of the paper is organized as follows. In Sect. 2 we describe the observations used in this study. In Sect. 3 we briefly discuss the spectroscopic techniques used in this paper. We also revisit the question of moss regions being the footpoints of hot loops in Sect. 4 using data from TRACE, EIS and the X-Ray Telescope (XRT; Golub et al. 2007). We discuss the thermal structure of moss regions in Sect. 5 followed by a discussion of density, filling factors and column depth in Sect. 6. We draw some conclusions in Sect. 7.

2. Observations

For this study, we have primarily used observations recorded by EIS aboard Hinode. EIS has an off-axis paraboloid design with a focal length of 1.9 m and mirror diameter of 15 cm. It consists of a multi-toroidal grating which disperses the spectrum onto two different detectors covering 40 Å each. The first detector covers the wavelength range 170–210 Å and the second covers 250–290 Å providing observations in a broad range of temperatures ($\log T \approx 4.7$ – 7.3). EIS has four slit/slot options available (1", 2", 40" and 266"). High spectral resolution images can be obtained by rastering with a slit.

An active region AR 10953, which appeared on the east solar limb on April 27, 2007, was observed by Hinode/EIS as it crossed the visible solar disk. From May 1 till May 5th it was observed using the study sequence CAM_ARTB_CDS_A designed by the authors. This study sequence takes about 20 min to raster a field of view of the Sun of $200'' \times 200''$ with an exposure time of 10 s using the 2" slit. It has 22 windows and is rich in spectral lines, which allows us to derive the physical plasma parameters simultaneously at different temperatures. The top panel of Fig. 1 displays the active region imaged by TRACE in its 171 Å channel. The over-plotted box shows the portion of the active region which was scanned by EIS with its 2" slit. The lower panel shows an EIS image in Fe XII $\lambda 195.12$ line. The vertical structure in the middle of the image, outlined by the contour and also marked with arrows, locates the moss regions discussed throughout the paper.

The datasets comprise a couple of rasters each day, but these were not necessarily taken sequentially. On May 03, the study sequence was run four consecutive times with a cadence of 20 min each. This provides an excellent opportunity to study the physical characteristics of the moss over an hour. We have used these four datasets to study the variation of plasma parameters such as electron temperature, density and filling factor. In addition we have taken one raster each day from May 01 to May 05

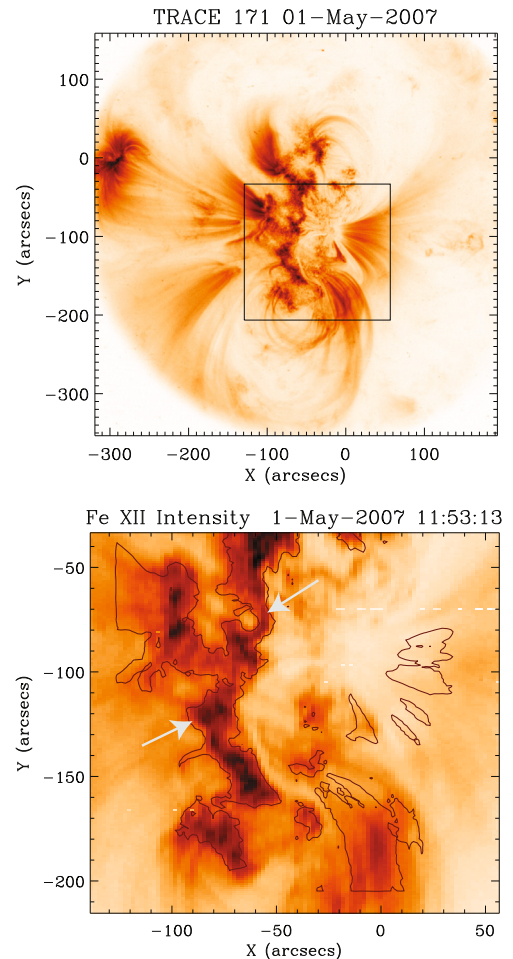


Fig. 1. *Top panel:* A TRACE image (plotted in a negative intensity scale) taken at 171 Å showing the active region studied in this paper. The over-plotted rectangle shows the region which was rastered on May 01 using the 2" slit of EIS. We note that a raster of this active region was obtained on 5 consecutive days with roughly the same coordinates of the boxed region. *Bottom panel:* an EIS image in Fe XII $\lambda 195.12$. The overplotted contours are from the TRACE intensity image. The vertical structure outlined with the contour in the middle of the image (also marked with arrows) is the moss region being discussed in the paper.

to study the variation in moss over a period of 5 days. In total we have analyzed 13 EIS datasets. Table 1 contains dates and the start times of EIS rasters used in this study.

Table 2 provides the list of spectral lines (formed at $\log T = 5.6$ – 6.5) used in this study. Four lines are affected by blending, but for three of the lines the blending component can be accurately estimated. Mg VII $\lambda 278.39$ is blended with Si VII $\lambda 278.44$ which has a fixed ratio relative to the unblended Si VII $\lambda 275.35$ line and so can be easily evaluated (see e.g., Young et al. 2007a). Fe XIV $\lambda 274.20$ is blended with Si VII $\lambda 274.18$ which is generally much weaker. We estimate the Si VII $\lambda 274.18$ contribution using Si VII $\lambda 275.35$ which has its highest ratio of 0.25 in a density region of 10^{10} cm $^{-3}$.

Fe XIII $\lambda 203.82$ is partly blended with Fe XII $\lambda 203.72$ and the two components can be extracted by simultaneously fitting two Gaussians to the observed spectral feature. Fe VIII $\lambda 186.60$ is blended with Ca XIV $\lambda 186.61$ but it is not possible to estimate the blending contribution using the available data. Since Ca XIV is formed at around $\log T = 6.6$, it will only be significant in the core of the active region, however this is where the moss regions

Table 1. Dates and raster start times of EIS data used in this study.

Date	Raster start times (UT)
01-May-2007	11:53:13
02-May-2007	05:06:11 18:31:20
03-May-2007	14:01:52 14:21:12 14:40:31 14:59:51
04-May-2007	06:37:17 06:56:36
05-May-2007	05:24:09 07:25:56 07:45:16 08:04:35

Table 2. Spectral lines (first column) from the study sequence “CAM_ARTB_CDS_A” chosen to derive the physical parameters in moss regions.

Line ID	Wavelength (Å)	$\log(N_e)$ range (cm ⁻³)	$\log(T_e)$ (K)
Fe VIII	186.60	–	5.6
Mg VII	278.39	–	5.8
Mg VII	280.75	8.0–11.0	5.8
Si VII	275.35	–	5.8
Fe IX	188.50	–	6.0
Fe XI	188.23	–	6.1
Si X	258.37	8.0–9.7	6.1
Si X	261.04	–	6.1
Fe XII	186.88	7.0–12.0	6.1
Fe XII	195.12	–	6.1
Fe XIII	196.54	9.3–11.0	6.2
Fe XIII	202.02	–	6.2
Fe XIII	203.83	8.0–10.5	6.2
Fe XIV	264.78	8.0–11.0	6.3
Fe XIV	274.20	–	6.3
Fe XV	284.16	–	6.4

Notes. The second column shows the central wavelengths, the third column shows the range of electron densities over which the ratios of lines are sensitive. Column four shows the peak formation temperature for the spectral lines.

are found and so Ca XIV can be expected to be a significant contributor to the Fe VIII line.

The Fe XII λ 186 and λ 195 lines are self blends. For Fe XII λ 186, we have fitted both of the lines with one Gaussian and we have used both spectral lines in the CHIANTI v6.0 (Dere et al. 1997, 2009) model in the derivation of the density. The Fe XII λ 195.12 line is self-blended with the Fe XII λ 195.18 line (Del Zanna & Mason 2005). The ratio of these two lines is sensitive to density. This blend can safely be ignored for quiet solar active region conditions such as for quiescent active region loops. However, the blend cannot be ignored while studying the moss regions, where the electron density is well above 10^{10} cm⁻³ and the line at λ 195.18 becomes ~15% of the line at λ 195.12. Young et al. (2009) suggested that to deal with the λ 195.18 blend a two Gaussian fit can be performed, where the stronger λ 195.12 line has free parameters for the centroid, width and intensity, while λ 195.18 is forced to be 0.06 Å towards the long wavelength side of λ 195.12, and to have the same line width as λ 195.12. However, the intensity of λ 195.18 is free to vary. In

this study, we have used the technique suggested by Young et al. (2009) to de-blend λ 195.12 from λ 195.18.

3. Spectroscopic techniques

In order to derive physical parameters such as temperature, electron density and filling factors, a number of different spectroscopic techniques can be applied to EIS observations. For a review of different spectroscopic techniques see e.g. Dere & Mason (1981) and Mason & Monsignori Fossi (1994).

The intensity of an optically thin emission line can be written as

$$I = 0.83 \text{ Ab}(z) \int_h G(T_e, N_e) N_e^2 dh \quad (1)$$

where $\text{Ab}(z)$ is the elemental abundances, T_e is the electron temperature, and N_e is the electron density. The factor 0.83 is the ratio of protons to free electrons which is a constant for temperatures above 10^5 K. $G(T_e, N_e)$ is the *contribution function* which contains all the relevant atomic parameters for each line, in particular the ionization fraction and excitation parameters and is defined as

$$G(T_e, N_e) = \frac{hc}{4\pi\lambda_{ij}} \frac{A_{ji}}{N_e} \frac{N_j(X^{+m})}{N(X^{+m})} \frac{N(X^{+m})}{N(X)} \quad (2)$$

where i and j are the lower and upper levels, A_{ji} is the spontaneous transition probability, $\frac{N_j(X^{+m})}{N(X^{+m})}$ is the population of level j relative to the total $N(X^{+m})$ number density of ion X^{+m} and is a function of electron temperature and density, $\frac{N(X^{+m})}{N(X)}$ is the ionization fraction which is predominantly a function of temperature. The contribution functions for the emission lines considered here were computed with version 6 of the CHIANTI atomic database (Dere et al. 2009) using the CHIANTI ion balance calculations and the coronal abundances of (Feldman 1992).

3.1. Determination of electron temperature

The solar plasma generally shows a continuous distribution of temperatures which is why such a broad range of ion species is seen in the solar spectrum. The distribution is usually expressed as an emission measure distribution that indicates the amount of plasma at each temperature. In some cases solar plasma is found to be very close to isothermal and an example is the quiet Sun plasma observed above the limb (Feldman et al. 1999). A method that is very effective for establishing if a plasma is isothermal is the so-called EM-loci method (see e.g. Jordan et al. 1987; Feldman et al. 1999; Del Zanna et al. 2002). In this method, the ratios of observed intensities of different spectral lines with their corresponding contribution functions and abundances (i.e., $I_{\text{obs}}/[Ab(z) G(T_e, N_e)]$) are plotted as a function of temperature. If the plasma is isothermal along the line-of-sight (LOS) then all of the curves would cross at a single location indicating a single temperature.

An indication of temperature can be obtained using emission lines from ions with different ionization stages. As contribution functions are generally sharply peaked functions in log temperature then ratios of two contribution functions will be monotonic functions in temperature, allowing observed intensity ratios to be converted to a temperature estimate. The temperature is not physically meaningful if the plasma is multithermal. However if the two ions are formed close to the dominant emission temperature of the plasma then the ratio will accurately reveal those

locations with more high temperature plasma and those with more low temperature plasma. For the present work we have used emission lines from Fe XI and Fe XIII (Sect. 5).

As the moss studied here is found to be multithermal it is necessary to perform an emission measure analysis to determine the temperature distribution. Here we follow the approach of Pottasch (1963) whereby individual emission lines yield estimates of the emission measure at the temperature of formation for each spectral line. By considering lines formed over a wide range of temperatures, an emission measure distribution can be determined. The method requires the contribution function to be approximated by a simplified function such that G is defined to be a constant, G_0 , over the temperature range $\log T_{\max} - 0.15$ to $\log T_{\max} + 0.15$ where T_{\max} is the temperature where the contribution function has its maximum. G_0 is evaluated as

$$G_0 = \frac{\int G(T_e, N_e) dT_e}{T_{\max} \times (10^{0.15} - 10^{-0.15})}. \quad (3)$$

The expression for the line intensity, Eq. (1), then becomes

$$I = 0.83Ab(z)G_0 \int N_e^2 dh. \quad (4)$$

The emission measure for the emission line is then defined as

$$EM = \int N_e^2 dh \quad (5)$$

and so

$$EM = \frac{I_{\text{obs}}}{0.83Ab(z)G_0} \quad (6)$$

thus the emission measure is defined entirely by the observed line intensity, the element abundances and the atomic parameters contained in G_0 .

An IDL routine called *integral_calc.pro* available in the CHIANTI software distribution is used here to compute the quantity G_0 .

3.2. Determination of electron density, filling factor and column depth

The electron density of an astrophysical plasma can be derived by measuring two emission lines of the same ion that have different sensitivities to the plasma density, the ratio yielding a direct estimate of the density (e.g. Mason & Monsignori Fossi 1994). This method is independent of the emitting volume, element abundances or ionization state of the plasma, and depends solely on the atomic population processes within the ion.

EIS provides access to a number of line ratio density diagnostics formed at different temperatures and Table 2 lists the diagnostics observed with the observation study *CAM_ARTB_CDS_A*. The theoretical variations of the line ratios with density are derived using version 6 of the CHIANTI database (Dere et al. 2009) and the curves are shown in Fig. 2.

The density can be used to derive the filling factor of the plasma. If we assume that the density is constant within the emitting volume for the ion then the emission measure (Eq. (5)) can be written as $N_e^2 h$ where h is the column depth of the emitting plasma. Rearranging Eq. (6) then gives

$$h = \frac{I_{\text{obs}}}{0.83Ab(z)G_0N_e^2}. \quad (7)$$

By inspecting images of the emitting plasma, it is possible to determine the apparent column depth of the plasma, h_{app} . In the

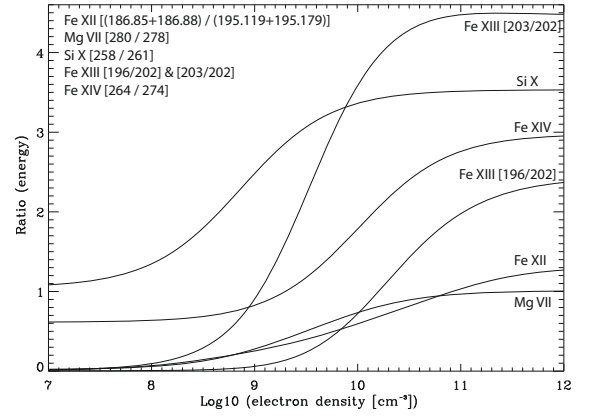


Fig. 2. CHIANTI, v6.0, theoretical intensity ratios with respect to electron density for the spectral line ratios used in this paper. The spectral lines are labelled on the plot.

present case this is done by studying images of the moss as the active region approaches the limb (Sect. 6). That is when the radial dimension of the moss is almost perpendicular to the line of sight and so its depth can be measured visually. The ratio of the spectroscopically derived column depth, h , to h_{app} then yields a value for the filling factor, ϕ , of the plasma, i.e.,

$$\phi = \frac{EM}{N_e^2 h_{\text{app}}}. \quad (8)$$

ϕ essentially measures the fraction of the observed plasma volume that is actually emitting the emission line under study. Values less than one imply that the volume is not completely filled with emitting plasma.

4. Active region moss and hot loops

Based on the observations recorded from TRACE and SXT and using analytical calculations it has been proposed that the moss regions are the footpoints of the hot loops seen in the SXT images taken at 3–5 MK. However, we note that the spatial resolution of TRACE is a factor of 2.5 better than the high resolution SXT images. The X-ray images recorded by XRT aboard Hinode are of comparable resolution to that of TRACE images (1 arcsec per pixel). In addition, spectral images obtained using EIS provide further information at intermediate temperatures. Hence, we have revisited this relationship question in this paper using TRACE, XRT and EIS observations.

In order to compare the observations taken from XRT, TRACE and EIS, a coalignment of the images was performed. It is known that images taken using the two CCDs of EIS are shifted with respect to each other (Young et al. 2007b). To coalign the EIS spectral images obtained from the two detectors, we cross-correlated images obtained in Fe XII $\lambda 195$ and Si X $\lambda 261$. Since the peak formation temperature of these two lines are the same, they reveal the same structures. The TRACE $\lambda 171$ and XRT Al_{poly} images were then cross-correlated with the images obtained in Fe XII $\lambda 195$ and Fe XV $\lambda 284$ respectively.

Figure 3 displays co-aligned images recorded from TRACE $\lambda 171$ (top left panel), EIS Fe XII (top right), EIS Fe XV (bottom left) and XRT (using the Al_{poly} filter) (bottom right panel). The images are displayed in a negative intensity scale. The bright moss regions can be seen as dark regions located in the left half of the top left image, as also shown in the bottom

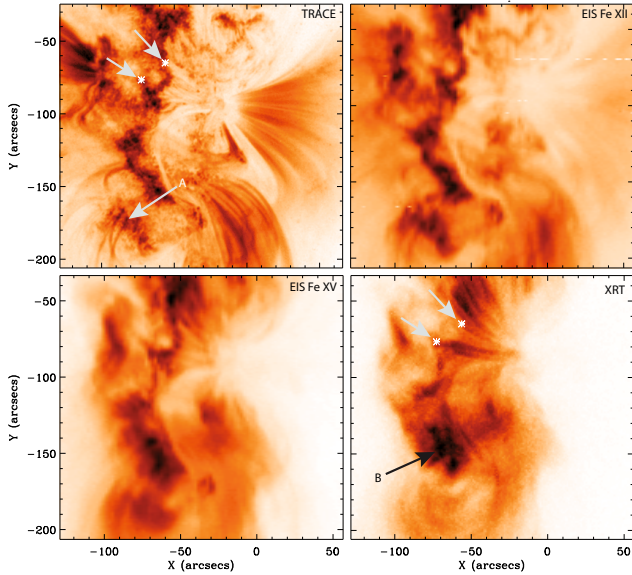


Fig. 3. Co-aligned TRACE $\lambda 171$ (top left), EIS Fe XII $\lambda 195$ (top right), EIS Fe XV $\lambda 284$ (bottom left) and XRT Al_{poly} filter images (bottom right) taken on May 01, 2007. The images are shown in negative intensity. The two stars indicated by two arrows in the TRACE image show moss regions. The two stars in the XRT image are located at the same position as those in the TRACE image showing the footpoints of hot loops. The arrow “A” locates a couple of 1MK loops rooted in moss regions. Arrow “B” in the XRT image shows the high temperature fuzzy emission in the moss regions.

panel of Fig. 1. We have plotted two asterisks on the TRACE image, shown by two arrows in the top left image, locating moss regions. The two asterisks in the bottom right image (also shown by two arrows) correspond to the same locations as those in the top right image. This clearly demonstrates that those moss regions are essentially located at the footpoints of the hot loops as deduced previously (see e.g., Antiochos et al. 2003). The arrow labelled as “A” in the top left panel locates a 1 MK loop located in the moss regions and coexistent with high temperature loops seen in EIS Fe XV and XRT images. Therefore, it appears reasonable to deduce that the moss regions are not just the footpoints of hot loops, rather there are warm loops at 1 MK which are also rooted in the moss regions. However, we cannot rule out the possibility that these warm loops are those which are cooling down to 1 MK from a temperature of 2–3 MK i.e., from XRT temperatures to TRACE.

The arrow labelled as “B” in the XRT image shows hot fuzzy emission, which is located over moss regions when compared to the top left image. The loop structures are not clear and it is difficult to deduce if these moss regions are the footpoints of loops.

5. Thermal structure of moss

The moss regions were originally noted in the images recorded using the 171 Å channel of TRACE, which primarily observes solar transition region plasma at a temperature of ~ 1 MK. Fletcher & de Pontieu (1999), using a DEM study of an observation taken from SoHO/CDS, showed that the plasma in moss regions was multi-thermal. Recent studies using EIS data (see e.g., Warren et al. 2008b; Tripathi et al. 2008) confirmed that moss regions are seen not only at 1 MK but in a range of temperatures. Therefore, in order to understand the physics of moss

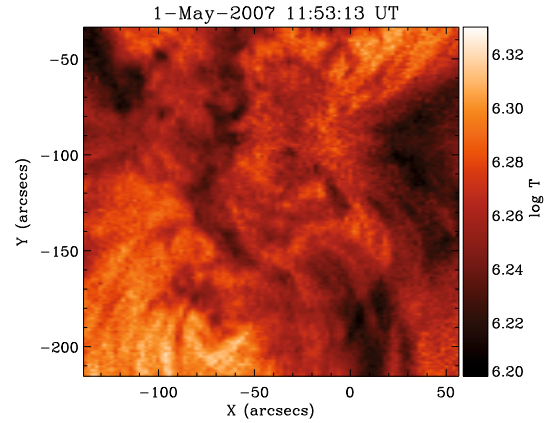


Fig. 4. A temperature map derived using intensity ratios of Fe XI $\lambda 188$ and Fe XIII $\lambda 202$. We used the ionization fraction from CHIANTI v6.0.

regions, it is important to understand the thermal structure of moss and its temporal variation.

Figure 4 displays a temperature map of the active region rastered on May 01, 2007 which was derived using intensity ratios of Fe XI $\lambda 188.2$ and Fe XIII $\lambda 202.0$ using the ionization fraction from CHIANTI v6.0 and the coronal abundances of Feldman (1992). The temperature map shows that most of the moss regions (corresponding to the contoured regions in the bottom panel of Fig. 1) is within the temperature range of $\log T = 6.2$ – 6.3 . This basically reflects the fact that by taking ratios, we are measuring a temperature common to the *contribution functions* of the two spectral lines. From the figure, however, it is evident that the moss regions are at a temperature of $\log T = 6.2$. In addition, we find that moss regions are cooler than some of the surrounding regions. Indeed, for those regions, we found the existence of hot emission by investigating the spectral images obtained in Fe XIV and Fe XV lines.

The bottom panel in Fig. 5 shows the “EM-loci” plots for one region (region 1) of the moss, labelled in the top panel. In order to compute the EM-loci plots, we have only used the spectral lines of iron, so that we can rule out any effects of abundance variations on the relative magnitudes of the emission measures obtained for different spectral lines. As can be deduced from the figure, the plasma along the LOS is multi-thermal. Most of the emission, however, is within the temperature range 1.2 MK to 1.8 MK. The peak of emission measure is at around $\log T = 6.2$, suggesting a similar temperature for the moss to that derived from the line ratios. For all the five regions marked in Fig. 5 (top panel), the crossing point of the curves are very similar. However, the magnitude of the emission measure crossing point is different for different regions. In order to check the variation in the thermal structure of the moss regions, we generated EM-loci plots of all 13 datasets listed in Table 1. The crossing points of the EM curves were similar to that shown in the bottom panel of Fig. 5, however the magnitude of the emission measure did vary from region to region. We also considered each raster for five consecutive days and traced a specific region in all of the rasters. The EM-loci plots obtained for each region for all five days showed remarkable similarities in terms of the crossing points of the curves. Therefore, we conclude that the thermal structure of the moss region remains fairly constant, at least for the active region studied in this paper and that most of the plasma in the moss region is in the temperature range 1.2 MK to 1.8 MK. Hence, the EM-loci plot presented in Fig. 5 can be taken as typical for all regions of moss in this study.

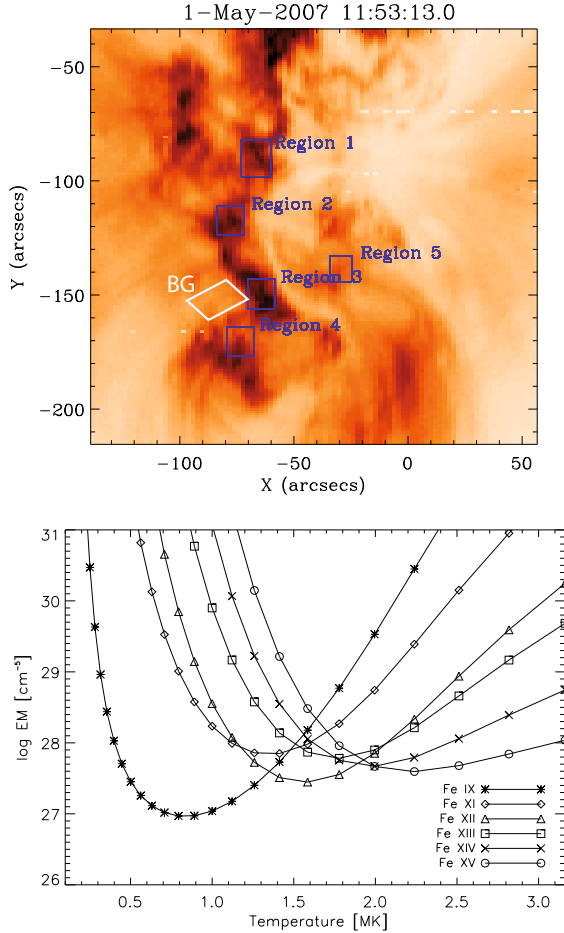


Fig. 5. *Top panel:* an Fe XII image from an EIS raster. The overplotted boxes show the regions which were used for deriving plasma parameters. BG is the region which was used to subtract the background emission in Sect. 6.2. *Bottom panel:* an EM-loci plot for region 1 using the ionization balance from CHIANTI v6.0 and the coronal abundances of Feldman (1992). The meaning of the different symbols are shown in the figure.

The EM-loci analysis indicates that the plasma along the LOS in the moss regions is multi-thermal. Therefore, in order to get a proper thermal structure, we need to perform an EM analysis. For this purpose we have used the Pottasch method as described in Sect. 3.1. Figure 6 shows a plot of the average EM for all of the five regions shown in the top panel of Fig. 5. The EM was calculated using ionization fraction from CHIANTI v6.0 and the coronal abundances of Feldman (1992). In addition, for Fe VIII and Fe IX we have used densities derived using Mg VII (formed at a similar temperature), for Fe XI and Fe XII we have used densities derived from Fe XII and for Fe XIII and Fe XIV we have used densities derived from diagnostic line ratios within those ions. As is evident from the plot, most of the emission in moss regions is observed in Fe XIII in all cases. The emission starts to decrease in Fe XIV and Fe XV. From the plot it appears that Fe XIII is the turning point of the emission measure curve. It is likely that the emission seen in Fe XIII is not just from the moss emission, but is possibly contaminated with emission from hot loops which are seen in Fe XIV and Fe XV. The plot shows very little difference in the emission seen in Fe VIII and Fe IX. This could be due to the fact that the Fe VIII $\lambda 186.6$ line used in this study is blended with another line, Ca XIV $\lambda 186.61$ formed at $\log T = 6.4$, and could therefore be contaminated with some

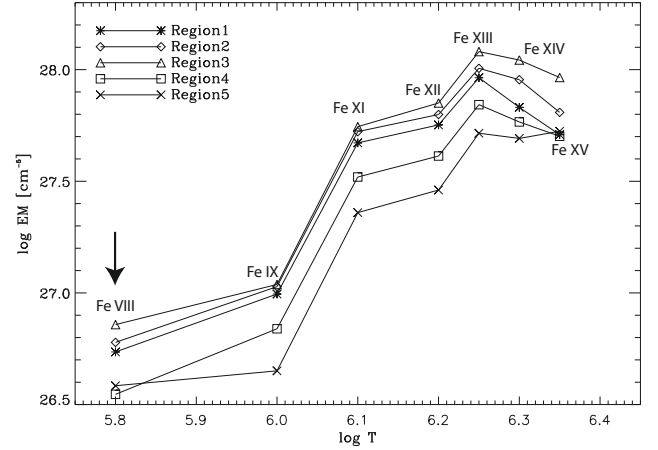


Fig. 6. An average emission measure plot for the five regions shown in the top panel of Fig. 5. CHIANTI v6.0 ionization equilibrium and the coronal abundances of Feldman (1992) were used. The EM derived for Fe VIII is an upper limit and is marked with an arrow.

emission from hot loops overlying the moss regions. The plot shown in Fig. 6 suggests that a temperature somewhat close to the formation temperature of Fe XI and Fe XIII ($\log T = 6.1$ – 6.3) is the characteristic temperature of the moss for this active region.

To study the variation of thermal structure in the moss regions over a period of five days, we have considered one raster every day and performed an emission measure analysis in a specific region. For the coalignment we cross-correlated the rasters obtained on consecutive days. Figure 7 shows the co-aligned intensity images for five consecutive days obtained in Fe XII $\lambda 195$. The data above the white lines in the last three images show the artifacts introduced due to cross-correlation and interpolation. We believe that we have achieved the co-alignment within a few arcsec. The overall structure of the active region stays almost the same. Figure 8 shows emission measure as a function of temperature for the boxed region shown in the left image in Fig. 7. As discussed earlier and shown in Fig. 6 most of the emission in the moss region comes from Fe XIII and the emission starts to decrease in Fe XIV. It can be easily seen from the plot that the average emission measure for the boxed region remains fairly constant over the five day period for all five spectral lines. This suggests that the thermal structure in the moss region does not change significantly with its temporal evolution.

6. Densities and filling factors in moss

6.1. Densities in moss regions

Figure 9 gives the densities measured in five different moss regions (shown in the top panel of Fig. 5) simultaneously at different temperatures using the spectral lines Mg VII ($\log T = 5.8$), Fe XII ($\log T = 6.2$), Fe XIII ($\log T = 6.25$), Fe XIV ($\log T = 6.3$). The uncertainties on the densities are calculated using 1-sigma errors in the intensities derived from a Gaussian fitting of the spectral lines and the photon statistics. In addition the errors for the derived electron densities from the theoretical CHIANTI curves are estimated. These are larger when the curves approach their high and low density limits. The plot demonstrates that the electron density in each moss region falls off with temperature except for that derived from Mg VII. However, we note the large error bars on the Mg VII densities. These large errors are due to the fact that the two Mg VII lines

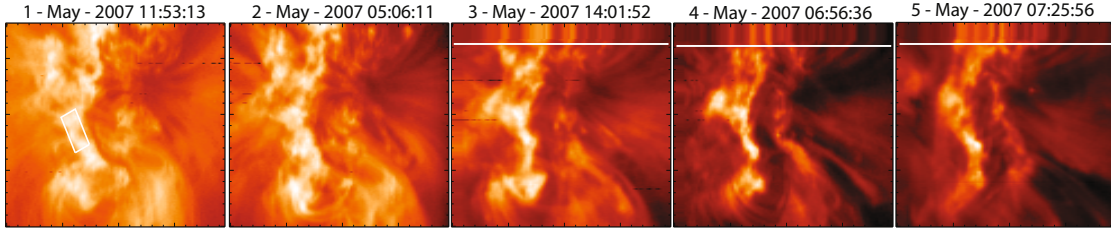


Fig. 7. Coaligned intensity images obtained in Fe XII $\lambda 195$ for five consecutive days. The box shown in the *left* most image is chosen to perform the emission measure analysis.

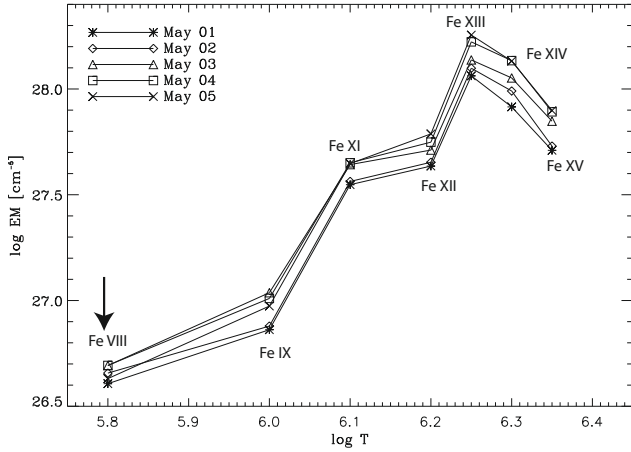


Fig. 8. An emission measure curve (obtained using the Pottasch method) for five days for the region shown in Fig. 7. CHIANTI v6.0 ionization equilibrium and the coronal abundances of Feldman (1992) were used. The EM for Fe VIII is an upper limit and is marked with an arrow.

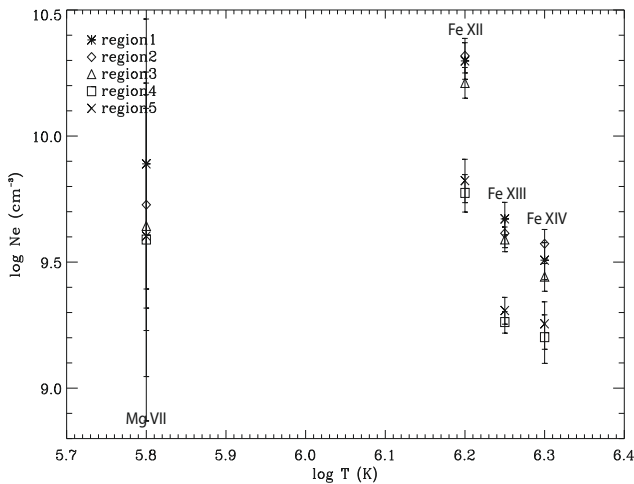


Fig. 9. Electron density measured using Mg VII, Fe XII, Fe XIII and Fe XIV for the five different regions marked in the top panel in Fig. 5.

in EIS active region spectra are very weak (see e.g., Young et al. 2007b). It is also worth pointing out that the densities obtained using Fe XII lines are much higher than those obtained using Fe XIII and Fe XIV. The decrease in the densities with temperature seen in the figure is anticipated if we assume a constant pressure in a given moss region. However, considering the peak formation temperature for each line and the corresponding derived densities we find that the pressure for Fe XII is substantially higher than those for Fe XIII and Fe XIV.

We have studied the short term and long term temporal variations of electron densities in the moss regions. For this purpose we have considered four consecutive rasters taken 20 min apart on May 03, 2007. Figure 10 displays the variation of electron

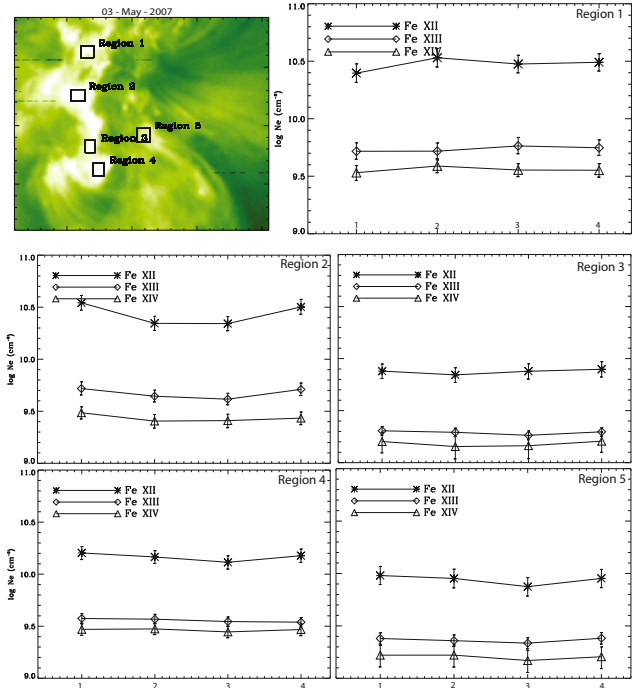


Fig. 10. The electron density variation in the moss regions over an hour derived from four consecutive EIS rasters.

densities derived using Fe XII, Fe XIII, and Fe XIV for the five regions shown in the top left panel of the figure. Electron density values for different rasters are plotted with different symbols in each plot. The error bars are estimated as in Fig. 9. The uncertainties in the densities obtained using Mg VII are very large, so we have omitted Mg VII from the plot. The density falls off with temperature in a similar way to the plot shown in Fig. 9. It is also clear from the plot that the densities obtained using Fe XII are consistently higher than those derived using Fe XIII and Fe XIV. The densities derived using Fe XIII are also always larger than those by Fe XIV. However, the small difference between the densities obtained from Fe XIII and Fe XIV could be real indicating constant pressure. The plots clearly demonstrate that there is almost no change in electron density over an hour at all three temperatures.

To study the evolution of electron density in the moss regions over a period of five days, we have considered the boxed region corresponding to the one shown in the left panel of Fig. 7. The density maps corresponding to the intensity maps shown in Fig. 7 are shown in Fig. 11. The box in the top left image in Fig. 11 corresponds to the region boxed in the intensity image shown in Fig. 7. As with the intensity images, the data above the white lines in the last three density maps shows an artifact introduced due to cross-correlation. As can be seen from the figure, the overall density structure stays fairly similar as does the intensity structure (see Fig. 7) with just a small enhancement in the center of the moss region. To show this quantitatively, we have

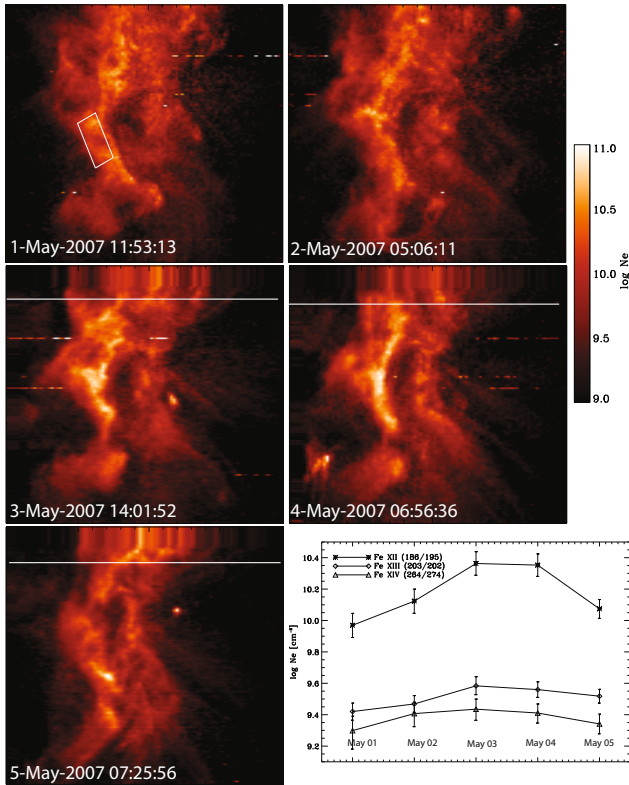


Fig. 11. Electron density maps obtained using coaligned intensity maps shown in Fig. 7. The *bottom right panel* displays the electron density variation over a period of five days measured using Fe XII, Fe XIII and Fe XIV for the boxed region shown in the *top left panel*.

studied the density variation in the boxed region shown in the top left image. The bottom right panel in Fig. 11 displays the density variation showing that the electron density increases from May 1 to May 3 and then decreases on May 4, which is quite pronounced in Fe XII and very slightly in Fe XIII and Fe XIV. Except for this enhancement, we find that the electron density remains fairly similar in the moss regions and does not show much variation in time. Although the reason for this enhancement in densities is not clear to us, we anticipate that this could be due to small scale dynamic activity taking place in the core of active regions seen in an XRT movie for this region. Using Coronal Diagnostic Spectrometer (CDS; Harrison et al. 1995) and Michelson Doppler Imager (MDI; Scherrer et al. 1995) data, Tripathi et al. (2006); Mason & Tripathi (2008) showed that localized enhancements in electron densities were correlated with emerging and canceling flux regions. We also note that canceling flux regions are frequently observed near the polarity inversion line (see e.g., Tripathi 2005). However, further investigation of this is needed.

In all of the measurements so far presented in this paper and those results presented in other papers for high density regions (that is densities greater than 10^9 cm^{-3}) cf. Tripathi et al. (2008); Warren et al. (2008b); Young et al. (2009); O'Dwyer et al. (2010), the densities measured using Fe XII are reported to be larger than those obtained from Fe XIII and Fe XIV. It is worth mentioning here that if the Fe XII $\lambda 186.8$ line were blended and we lower the intensity by 20%, the electron densities obtained using Fe XII would become consistent with those obtained using Fe XIII and Fe XIV. However, we cannot at present explain these discrepancies and so we leave this as an open question.

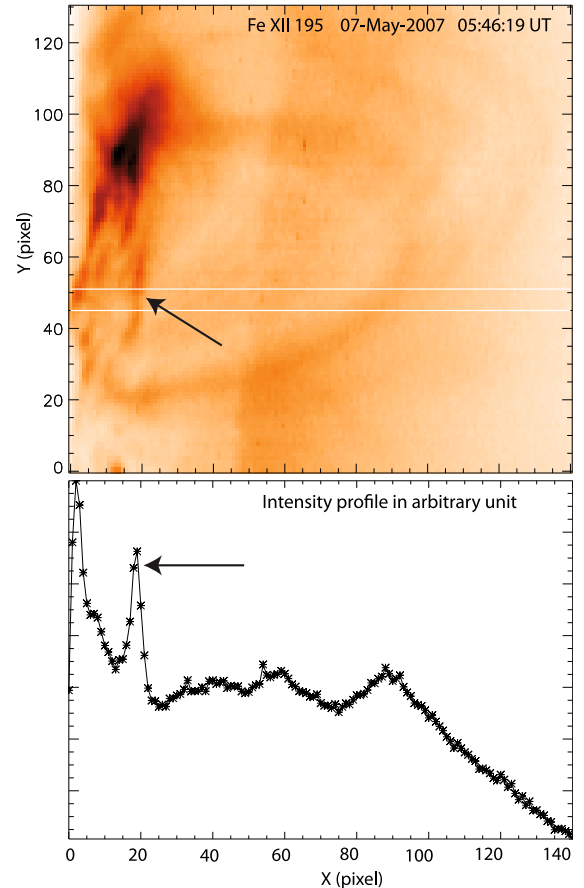


Fig. 12. *Top panel:* Negative intensity image for Fe XII $\lambda 195$ on 07-May-2007. *Bottom Panel:* the intensity profile for Fe XII $\lambda 195$ between the two lines marked in the *top panel*. The arrow in the *top panel* marks the moss region and in the *bottom panel* marks the intensity enhancement due to the moss region.

6.2. Filling factors in moss regions

Equation (8) gives the expression for deriving the filling factor from the emission measure, density and apparent column depth. The emission measure and density are derived directly from the spectroscopic data as described in the previous sections. To estimate the apparent column depth we follow the method of Martens et al. (2000) and study images of the moss at the solar limb. The active region was observed close to the limb with EIS on 2007 May 7 and radial intensity profiles cutting through a particular moss region were studied in lines of Fe XII, Fe XIII and Fe XIV. A sample intensity profile from Fe XII $\lambda 195.12$ is shown in Fig. 12 where a distinctive spike in emission corresponding to the moss region can be seen. We interpret the width of this spike to be the column depth of the moss, which is found to be $6''$ ($\sim 4000 \text{ km}$) in this case, in good agreement with the results of Martens et al. (2000).

Table 3 shows electron densities, filling factors and the column depths for five different regions shown in the top panel in Fig. 5 using the ions Fe XII, Fe XIII and Fe XIV before and after background subtraction. We have used the region labelled “BG” in the top panel of Fig. 5 for background/foreground subtraction. The filling factor is estimated using Eq. (8). The column depth is estimated using Eq. (7) assuming a filling factor equal to 1. The table clearly demonstrates the importance of background/foreground in the measurements of electron densities and filling factors. The electron densities for each ion have increased substantially after subtracting the background, and the

Table 3. Density (N_e), column depth (h) and filling factor (ϕ) measurements for five moss regions shown in Fig. 5.

Before background subtraction									
	Fe XII			Fe XIII			Fe XIV		
	$\log N_e$	h	ϕ	$\log N_e$	h	ϕ	$\log N_e$	h	ϕ
	(cm^{-3})	(km)		(cm^{-3})	(km)		(cm^{-3})	(km)	
Region1	10.32 ^{10.39} _{10.25}	140 ¹⁰⁰ ₂₀₀	0.04	9.73 ^{9.76} _{9.70}	3000 ²⁷⁰⁰ ₃₃₀₀	0.8	9.54 ^{9.60} _{9.48}	5600 ⁴⁴⁰⁰ ₇₁₀₀	1.4
Region2	10.32 ^{10.39} _{10.26}	160 ¹²⁰ ₂₁₀	0.04	9.68 ^{9.71} _{9.66}	4200 ³⁸⁰⁰ ₄₃₀₀	1.0	9.57 ^{9.62} _{9.51}	6600 ⁵⁴⁰⁰ ₈₄₀₀	1.6
Region3	10.22 ^{10.28} _{10.15}	280 ²²⁰ ₃₉₀	0.07	9.63 ^{9.65} _{9.60}	6400 ⁶⁰⁰⁰ ₆₉₀₀	1.6	9.45 ^{9.50} _{9.40}	14000 ¹¹⁰⁰⁰ ₁₇₀₀₀	3.5
Region4	9.79 ^{9.86} _{9.72}	1200 ⁸⁰⁰ ₁₅₀₀	0.3	9.33 ^{9.36} _{9.30}	14000 ¹³⁰⁰⁰ ₁₅₀₀₀	3.5	9.21 ^{9.29} _{9.12}	22000 ¹⁶⁰⁰⁰ ₃₃₀₀₀	5.6
Region5	9.83 ^{9.91} _{9.74}	680 ⁵⁰⁰ ₁₀₀₀	0.2	9.37 ^{9.41} _{9.34}	8800 ⁷⁷⁰⁰ ₉₅₀₀	2.2	9.25 ^{9.33} _{9.15}	16000 ¹¹⁰⁰⁰ ₂₄₀₀₀	3.9
After background subtraction									
Region1	11.00 ^{11.08} _{10.93}	8 ⁶ ₁₀	0.002	10.58 ^{10.63} _{10.54}	130 ¹⁰⁰ ₁₅₀	0.03	10.04 ^{10.08} _{10.00}	720 ⁶²⁰ ₈₃₀	0.2
Region2	10.88 ^{10.95} _{10.82}	15 ¹⁰ ₂₀	0.004	10.17 ^{10.19} _{10.14}	970 ⁹³⁰ ₁₁₀₀	0.2	9.87 ^{9.90} _{9.83}	1900 ¹⁷⁰⁰ ₂₂₀₀	0.5
Region3	10.60 ^{10.65} _{10.55}	60 ⁵⁰ ₇₀	0.01	9.90 ^{9.92} _{9.88}	3200 ³⁰⁰⁰ ₃₃₀₀	0.8	9.62 ^{9.65} _{9.59}	6900 ⁶²⁰⁰ ₇₇₀₀	1.7
Region4	10.17 ^{10.22} _{10.12}	230 ¹⁹⁰ ₂₉₀	0.1	9.55 ^{9.57} _{9.53}	7500 ⁷²⁰⁰ ₇₉₀₀	1.9	9.48 ^{9.52} _{9.43}	7100 ⁶¹⁰⁰ ₈₇₀₀	1.8
Region5	10.91 ^{11.00} _{10.82}	7 ⁵ ₁₁	0.002	10.39 ^{10.45} _{10.34}	250 ²⁰⁰ ₃₀₀	0.1	9.71 ^{9.75} _{9.67}	2300 ²⁰⁰⁰ ₂₆₀₀	0.6

Notes. The box labelled as BG in the top panel of Fig. 5 was considered for background subtraction. The upper and lower case numbers indicate the errors.

filling factors and column depths have substantially decreased. This is the first time the importance of background/foreground emission has been demonstrated while estimating physical parameters such as density, filling factors and column depth in moss regions. After the background subtraction, we find substantial increases in the electron densities and meaningful results for filling factors. The filling factors derived for Fe XII are very low i.e., much less than 1, whereas those for Fe XIII and Fe XIV are closer to 1, sometimes even more than 1. A filling factor greater than 1 does not give any meaningful information. However, in the present case it suggests that we have very likely underestimated the column depth by using the thickness of the moss measured using TRACE observations.

The column depth measurements presented in Table 3, which are based on the assumption that the filling factor is 1, show that the moss seen in Fe XII is a very thin region i.e., about the order of a few tens of kilometers in the dense moss regions. At higher temperatures e.g., in Fe XIII and Fe XIV, the estimated column depth is larger than that estimated by Fe XII, by a large factor of ≈ 10 –20. One possible reason for this difference could be that the background/foreground is not completely removed. This could explain the higher filling factor and larger path length obtained for Fe XIII and Fe XIV. However, the question remains as to why we have such a small column depth for Fe XII in comparison to that which is measured from the limb observations. We note that the densities observed using Fe XII are too high in comparison to those derived using Fe XIII and Fe XIV and this is the most likely the reason for very low column depth. However, this complex issue involving atomic physics calculations needs further investigation in order to understand the discrepancies in densities, filling factors and column depth between Fe XII and other ions.

It is worthwhile emphasizing here that column depths and filling factors are derived using the coronal abundances of Feldman (1992). These values are significantly different (a factor of ~ 3 –4 larger) when photospheric abundances are used.

7. Summary and conclusions

Using Hinode/EIS observations, we have studied basic physical plasma parameters such as temperature, electron density, filling

factors, and column depth in moss regions and the variation of these parameters over an hour and over a time period of five days. In addition, we have revisited the question of whether the moss regions are the footpoints of hot loops using observations from TRACE, EIS and XRT. The results are summarized below.

- Based on the TRACE, EIS and XRT observations we find that most of the moss regions are essentially located at the footpoints of hot loops. In some places we observed TRACE 171 (1 MK) loops rooted in the moss regions.
- Based on the line intensity ratios of Fe XI $\lambda 188$ and Fe XIII $\lambda 202$, and an emission measure analysis, we find that the characteristic temperature of moss regions is about $\log T = 6.2$. Emission measure analyses over a time period of one hour (Fig. 6) and over five days (Fig. 8) reveal that the thermal structure of the moss regions does not change significantly with time.
- The electron densities measured using Fe XII ratios are about $1\text{--}3 \times 10^{10} \text{ cm}^{-3}$ and about $2\text{--}4 \times 10^9 \text{ cm}^{-3}$ using Fe XIII and Fe XIV. Work is in progress to try to resolve this discrepancy. It is worth emphasizing here that if the Fe XII $\lambda 186.8$ were blended and we lower its intensity by 20%, then the electron densities obtained using Fe XII would become consistent with those obtained using Fe XIII and Fe XIV. The densities derived using Fe XIII and Fe XIV are similar to those derived by Fletcher & de Pontieu (1999) using Si X line ratios observed by CDS. However, when we subtract the foreground/background emission we find a substantial increase (a factor of 3–4 or even more in some cases) in the densities.
- The electron densities only show small changes ($\sim 25\%$) over a period of an hour. There are large variations (an order of magnitude increase) in Fe XII densities when measured over a period of five days. However, the variation in the densities obtained using Fe XIII and Fe XIV is only about 50–70%.
- The filling factor of the moss plasma is in the range 0.1–1 and the path length along which the emission originates is from a few 100 to a few 1000 kms long.

These new measurements of the thermal and density structure in moss regions should provide important constraints for the modelling of loops in the hot and dense core of active regions.

Acknowledgements. We thank the referee for the constructive and thoughtful comments. D.T., H.E.M. and G.D.Z. acknowledge the support from STFC. We thank Brendan O'Dwyer for various discussions. Hinode is a Japanese mission developed and launched by ISAS/JAXA, collaborating with NAOJ as a domestic partner, NASA and STFC (UK) as international partners. Scientific operation of the Hinode mission is conducted by the Hinode science team organized at ISAS/JAXA. This team mainly consists of scientists from institutes in the partner countries. Support for the post-launch operation is provided by JAXA and NAOJ (Japan), STFC (UK), NASA (ESA), and NSC (Norway). The help and support of the Hinode/EIS team in particular is acknowledged.

References

- Antiochos, S. K., Karpen, J. T., DeLuca, E. E., Golub, L., & Hamilton, P. 2003, *ApJ*, 590, 547
- Berger, T. E., de Pontieu, B., Fletcher, L., et al. 1999, *Sol. Phys.*, 190, 409
- Culhane, J. L., Harra, L. K., James, A. M., et al. 2007, *Sol. Phys.*, 243, 19
- Del Zanna, G., & Mason, H. E. 2003, *A&A*, 406, 1089
- Del Zanna, G., & Mason, H. E. 2005, *A&A*, 433, 731
- Del Zanna, G., Landini, M., & Mason, H. E. 2002, *A&A*, 385, 968
- Dere, K. P., & Mason, H. E. 1981, in *Solar Active Regions: A monograph from Skylab Solar Workshop III*, ed. F. Q. Orrall, 129
- Dere, K. P., Landi, E., Mason, H. E., Monsignori Fossi, B. C., & Young, P. R. 1997, *A&AS*, 125, 149
- Dere, K. P., Landi, E., Young, P. R., et al. 2009, *A&A*, 498, 915
- Feldman, U. 1992, *Phys. Scr*, 46, 202
- Feldman, U., Doschek, G. A., Schühle, U., & Wilhelm, K. 1999, *ApJ*, 518, 500
- Fletcher, L., & de Pontieu, B. 1999, *ApJ*, 520, L135
- Golub, L., Deluca, E., Austin, G., et al. 2007, *Sol. Phys.*, 243, 63
- Handy, B. N., Acton, L. W., Kankelborg, C. C., et al. 1999, *Sol. Phys.*, 187, 229
- Harrison, R. A., Sawyer, E. C., Carter, M. K., et al. 1995, *Sol. Phys.*, 162, 233
- Jordan, C., Ayres, T. R., Brown, A., Linsky, J. L., & Simon, T. 1987, *MNRAS*, 225, 903
- Kosugi, T., Matsuzaki, K., Sakao, T., et al. 2007, *Sol. Phys.*, 243, 3
- Martens, P. C. H., Kankelborg, C. C., & Berger, T. E. 2000, *ApJ*, 537, 471
- Mason, H. E., & Monsignori Fossi, B. C. 1994, *A&A Rev.*, 6, 123
- Mason, H. E., & Tripathi, D. 2008, *Active Region Diagnostics*, ed. B. N. Dwivedi, & U. Narain, 127
- O'Dwyer, B., Del Zanna, G., Mason, H. E., et al. 2010, *A&A*, accepted
- Peres, G., Reale, F., & Golub, L. 1994, *ApJ*, 422, 412
- Pottasch, S. R. 1963, *ApJ*, 137, 945
- Scherrer, P. H., Bogart, R. S., Bush, R. I., et al. 1995, *Sol. Phys.*, 162, 129
- Schrijver, C. J., Title, A. M., Berger, T. E., et al. 1999, *Sol. Phys.*, 187, 261
- Tripathi, D. 2005, PhD Thesis, Max-Planck-Institute for Solar System Research, 37191 Katlenburg-Lindau Germany
- Tripathi, D., Mason, H. E., & Young, P. R. 2006, in *SOHO-17. 10 Years of SOHO and Beyond*, ESA SP, 617
- Tripathi, D., Mason, H. E., Young, P. R., & Del Zanna, G. 2008, *A&A*, 481, L53
- Tripathi, D., Mason, H. E., Dwivedi, B. N., del Zanna, G., & Young, P. R. 2009, *ApJ*, 694, 1256
- Tsuneta, S., Acton, L., Bruner, M., et al. 1991, *Sol. Phys.*, 136, 37
- Warren, H. P., Ugarte-Urra, I., Doschek, G. A., Brooks, D. H., & Williams, D. R. 2008a, *ApJ*, 686, L131
- Warren, H. P., Winebarger, A. R., Mariska, J. T., Doschek, G. A., & Hara, H. 2008b, *ApJ*, 677, 1395
- Young, P. R., Del Zanna, G., Mason, H. E., et al. 2007a, *PASJ*, 59, 857
- Young, P. R., Del Zanna, G., Mason, H. E., et al. 2007b, *PASJ*, 59, 727
- Young, P. R., Watanabe, T., Hara, H., & Mariska, J. T. 2009, *A&A*, 495, 587